Article

A high-performance genetically encoded sensor for cellular imaging of PKC activity in vivo

Takaki Yahiro [1,2], Landon Bayless-Edwards [1,2], James A. Jones[1], Yizhou Zhuo[1], Lei Ma[1], Maozhen Qin[1], Tianyi Mao [1] ✉ & Haining Zhong [1] ✉

Neuromodulators impose powerful control over brain function via their regulation of intracellular signaling through G-protein coupled receptors. In contrast to those of Gs and Gi pathways, in vivo imaging of the signaling events downstream of Gq-coupled receptors remains challenging. Here, we introduce CKAR3, a genetically encoded fluorescence lifetime sensor that reports the activity of protein kinase C (PKC), a major downstream effector of the Gq pathway. CKAR3 exhibits a lifetime dynamic range 5-fold larger than any existing PKC sensor. It specifically detects PKC phosphorylation with seconds kinetics without perturbing neuronal functions. In vivo two-photon lifetime imaging of CKAR3 reveals tonic PKC activity in cortical neurons. Animal locomotion elicits robust PKC activity in sparse neuronal ensembles in the motor cortex. Both basal and locomotion-elicited PKC activities are in part mediated by muscarinic acetylcholine receptors. Overall, CKAR3 enables interrogation of Gq signaling dynamics mediated by PKC in behaving animals.

Neuromodulators play critical roles in controlling animal behavior by activating G-protein coupled receptors (GPCRs) of three classes, namely Gs-, Gi- and Gq-coupled receptors, to modulate conserved intracellular signaling pathways[1–4]. Specifically, Gq-coupled neuromodulators, such as acetylcholine and serotonin, regulate animal arousal, attention, memory, cognition, and hallucination[5–10]. At present, microdialysis, voltammetry, and recently-developed genetically encoded sensors have enabled the detection of these neuromodulators in vivo during animal behavior[11–13]. However, multiple neuromodulators are commonly present in the brain and the modulation of each neuron is the integrated actions of all the modulators at a given moment. Furthermore, individual neurons may exhibit different downstream responses to the same extracellular neuromodulators via differentially expressed receptor subtypes. There is currently little appreciation of cell-specific signaling heterogeneity and dynamics downstream of Gq receptors in vivo.

The protein kinase C (PKC) family of serine/threonine kinases is a major downstream effector and signaling hub of the Gq pathway[14,15]. The Gq protein activates phospholipase C to produce diacylglycerol

(DAG) and inositol trisphosphate (IP3)[2,4]. DAG activates PKC, which can be potentiated by calcium mobilized from intracellular calcium stores by IP3. Additional cell-specific control in Gq-driven PKC signaling may arise from synaptic transmission and action potential activities, which also affect the level of intracellular calcium. Activated PKC then goes on to phosphorylate a variety of substrates to control neuronal excitability, synaptic transmission, neurotransmitter trafficking, and neuronal plasticity[16–23]. Given its central role in Gq signaling, understanding the spatiotemporal dynamics of PKC in vivo, during ongoing circuit activity, is critical to dissect how Gq neuromodulation controls neuronal function and animal behavior.

Several sensors have been developed to measure the spatiotemporal dynamics of PKC activity[23–28]. Although these sensors have been used to study PKC biology in vitro[23,28–30], they have not been successfully applied in vivo, in part due to limited dynamic range. We sought to develop a PKC sensor with sufficient dynamic range to capture in vivo PKC dynamics.

Herein, following the blueprint for the recent development of intracellular signaling sensors[31–33], we focus on developing a sensor

[1]Vollum Institute, Oregon Health and Science University, Portland, OR, USA. [2]These authors contributed equally: Takaki Yahiro, Landon Bayless-Edwards.
✉e-mail: mao@ohsu.edu; zhong@ohsu.edu

compatible with two-photon fluorescence lifetime imaging microscopy (2pFLIM). 2pFLIM offers advantages for in vivo imaging because it is relatively insensitive to variable expression levels, sample drifting, and wavelength-dependent light scattering[31,33,34]. We first screen previously developed PKC sensors[23–27] for their lifetime responses under identical conditions. We select the most promising one, C-kinase activity reporter 2 (CKAR2), and further engineer it to derive CKAR3. CKAR3 exhibits a dynamic range tenfold larger than CKAR2 and 5 times larger than any tested sensors. It detects specifically the phosphorylation by PKC and exhibits kinetics on the order of seconds. Experiments in cultured and acute slices reveal that CKAR3 enables the detection of Gq activation by the physiological neuromodulator acetylcholine without affecting neuronal physiology. When expressed in vivo, 2pFLIM imaging of CKAR3 reveals a tonic level of PKC activity at rest. Animal locomotion elicits robust CKAR3 responses in a sparse subset of layer 2/3 neurons in the primary motor cortex (M1) but not in other examined cortices. These neurons can be divided into two previously unappreciated classes with distinct PKC dynamics. Overall, our work establishes in vivo interrogation of PKC dynamics and heterogeneity during animal behavior.

Results

Comparison of PKC sensors and development of CKAR3

To develop a sensor for in vivo studies, we followed the steps from recent efforts for improving other signaling sensors[31,32]. We first compared existing PKC sensors (Fig. 1a) in human embryonic kidney (HEK) 293 cells using 2pFLIM. The maximal responses of these sensors, as elicited by the PKC activator phorbol 12,13-dibutyrate (PDBu, 1 μM) and the calcium ionophore ionomycin (1 μM), were relatively small (Fig. 1b−d and Supplementary Fig. 1). Among these sensors, IDOCKS (PKCα variant) gave the largest signal, but it involves the overexpression of a functional PKC isozyme. CKAR2 gave the second largest response, and its expression is likely benign because it is a PKC substrate without physiological function. We therefore focused on optimizing CKAR2.

CKAR2 uses the FHA1 phosphopeptide-binding domains[26,35]. Upon phosphorylation of a PKC substrate sequence within the sensor[36,37], the FHA1 domain binds to the phosphorylated peptide. This conformational reorganization alters Förster resonance energy transfer (FRET) between the cyan and yellow fluorescent proteins (FPs) at two ends of the sensor (Fig. 1a) to result in a changed lifetime of the donor fluorophore. To increase the sensor dynamic range, we attempted several
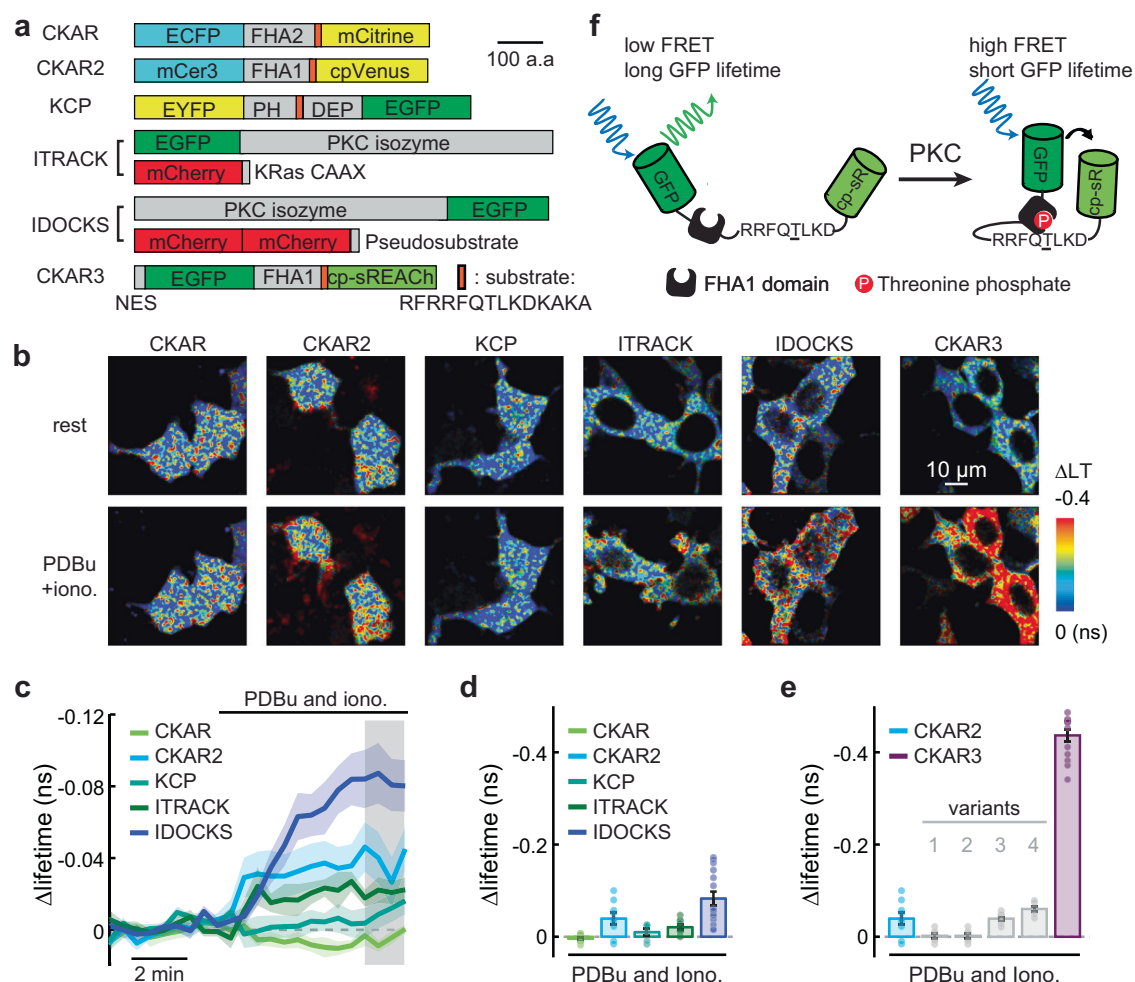

Fig. 1 | Development of CKAR3 in cultured cells. a Schematic of previous FRET-based PKC sensors and CKAR3. FHA1 and FHA2: Forkhead-associated domains 1 and 2, respectively; PH: Pleckstrin homology domain; DEP: disheveled, Egl-10, pleckstrin; NES: nucleus exportation sequence. **b** Representative Δlifetime images of the tested sensors at rest and after stimulation with 1 μM PDBu and 1 μM ionomycin (iono.). **c** Averaged response (ΔLT) traces of existing sensors. Quantification of existing sensors (**d**; at the gray window of panel **c**) and candidate variants (**e**). From left to right, n (cells/coverslip) = 11/4, 9/4, 6/3, 10/4, and 15/6 in panel (**d**), and 9/4, 7/3, 7/3, 10/3, 6/3, and 14/4 in panel **e**. **f**, Schematic of CKAR3 sensor. Note that only a partial substrate sequence was included in the schematic due to space constraints. The schematic was modified from (**a**) in ref. 31 with permission. Where applicable throughout the figure, mean (dark lines and bars) and s.e.m. (shaded area and error bars) are shown. Source data are provided as a Source Data file.
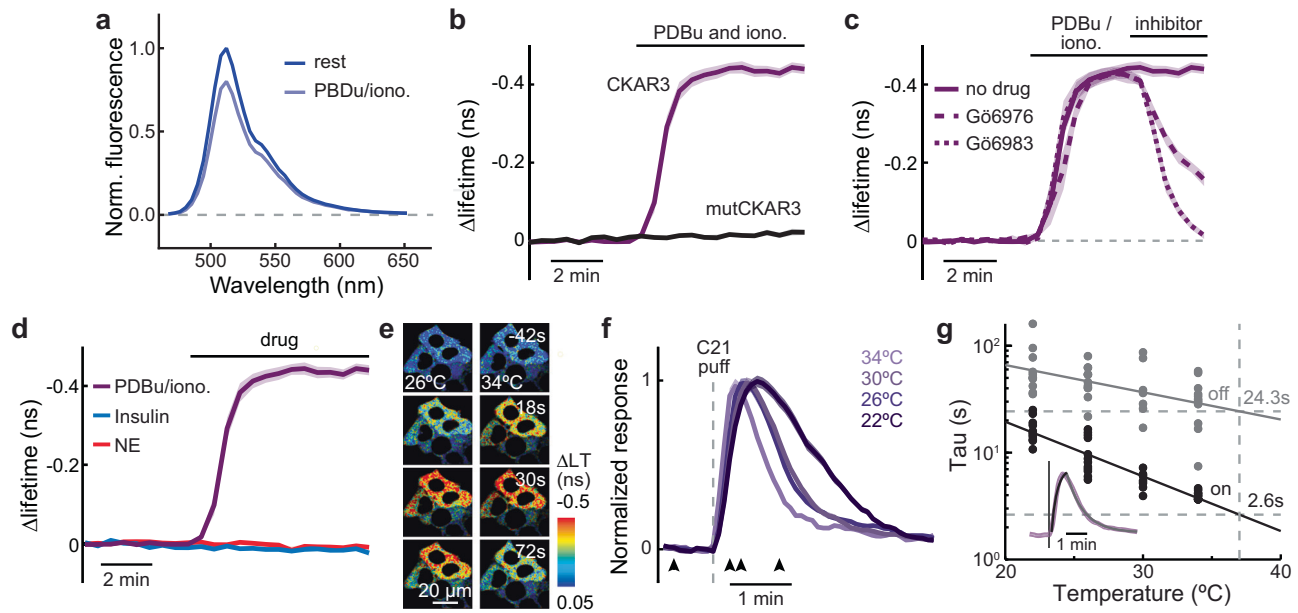
Fig. 2 | Characterization of CKAR3 in cultured cells. a CKAR3 emission spectrum inside HEK cells. n (cells/cultures) = 40/4. **b** Response traces of CKAR3 and mutCKAR3 to PDBu and ionomycin. n (cells/coverslips) = 14/4 and 11/4 for CKAR3 and mutCKAR3, respectively. **c** Responses of CKAR3 to PDBu and ionomycin followed by indicated antagonists. n (cells/coverslips) = 14/4, 7/3, and 8/3 for no drug, Gö6976, and Gö6983, respectively. **d** Responses of CKAR3 to the indicated stimulus. n (cells/coverslips) = 14/4, 7/3, and 10/4 for PDBu, insulin, and norepinephrine (NE), respectively. Representative images (**e**) and traces (**f**) and collective on and off tau (**g**) of CKAR3 responding to hM3D activation at the indicated temperatures. From hot to cold, n (cells/coverslips) = 12/4, 7/4, 12/4,11/3. Inset in panel (**g**): An example trace and its fitting. Where applicable throughout the figure, mean (dark lines and bars) and s.e.m. (shaded area and error bars) are shown. Source data are provided as a Source Data file.

strategies while keeping intact the FHA1 domain and substrate sequence of CKAR2 (Supplementary Fig. 2), including (i) using mTurquoise2[38] as the donor FP to increase the Förster distance (R_0) of FRET (variants 1–4), (ii) using tandem-dimer cpVenus to increase FRET efficiency (variants 1 and 3)[39], and (iii) switching the FPs to mEGFPΔ and cp-sREACh[40,41] and including a nucleus exportation sequence, similar to those of the analogous lifetime-only sensor for protein kinase A (PKA), tAKARβ[31]. The first two strategies resulted in little improvements under lifetime imaging (Fig. 1e). However, the third strategy greatly enhanced the lifetime signal (Δlifetime = -0.43 ± 0.003; ~11 fold larger than CKAR2, and ~5 fold larger than IDOCKS; Fig. 1d). This signal amplitude suggests great potential of the variant, as it is comparable to that of the PKA sensor tAKARα, which is sufficient for in vivo imaging[31]. We named it CKAR3 (Fig. 1f).

Characterization of CKAR3 in cultured cells

We extensively characterized CKAR3, first in HEK cells. As expected from its dark FRET acceptor (sREACh)[40,41], the emission and excitation spectra of CKAR3 resembled that of mEGFP (Fig. 2a and Supplementary Fig. 3a; see "Methods"). Stimulation with PDBu and ionomycin moderately reduced its intensity without significantly altering the spectrum, consistent with a shortened lifetime upon activation. Its lifetime dynamic range was stable across a broad range of wavelengths (Supplementary Fig. 3b). The sensor lifetime was resistant to intensity variations, such as drifting to different z-planes or different expression levels (Supplementary Fig. 3c, d). It was also largely resistant to pH variations from 6 to 8.5 (Supplementary Fig. 3e, f) when using nigericin (5 μM, a K+/H+ ionophore) to relay the bath pH to the inside of the cell[42].

We then tested the sensor specificity. A T-to-A mutation at the phosphorylation site (T416A; construct called mutCKAR3) eradicated the response to PDBu-ionomycin (Fig. 2b). In addition, CKAR3 responses were reverted by bath application of the broad-spectrum PKC inhibitor Gö6983 (1 μM) (Fig. 2c). Interestingly, the PKCα and PKCβ specific inhibitor Gö6976 (1 μM) only partially reverted the response (Fig. 2c). CKAR3 was also partially activated by PDBu when pretreated with Gö6976 but not with Gö6983 (Supplementary Fig. 3g). Additionally, CKAR3 did not respond to treatments of norepinephrine or insulin, which would activate PKA or protein kinase B (Akt/PKB)[31,43], respectively (Fig. 2d). Together, these results indicate that the CKAR3 response is specific to PKC phosphorylation mediated by multiple PKC isoforms.

To determine the sensor kinetics, we co-expressed the Gq-coupled hM3D receptor together with CKAR3. Using short puffs (1-s long) of the ligand C21, we found that the sensor exhibited temperature-dependent on- and off-kinetics with Q10 values of 3.3 and 1.8, respectively (Fig. 2e–g). By extrapolation, the sensor was estimated to exhibit a τ_{on} of 2.6 ± 1.7 s (fit ± 95% confidence level) and a τ_{off} of 24.3 ± 2.7 s at 37 °C. These values were likely overestimations because it was impossible to use instantaneous puffs, and the stimulant took time to dissipate. Finally, we found that, consistent with recent reports[44,45], 36% of CKAR3-expressing cells responded to ATP application (25 μM), and these responses were abolished by the Gq-coupled P2Y11 receptor[46] antagonist NF-157 (1 μM) (Supplementary Fig. 4). Together, these results indicate that CKAR3 responds to Gq activation of PKC.

Characterization of CKAR3 in neuronal tissue

To test CKAR3's performance in neurons, we first expressed it in cultured hippocampal slices using the biolistic transfection method. CKAR3 exhibited robust responses to acetylcholine (20 μM) in CA1 neurons, much larger than those from CKAR and CKAR2 under the same conditions (Fig. 3a–c). These responses were abolished by pretreatment of the broad spectrum muscarinic acetylcholine receptor (mAChR) antagonist scopolamine (1 μM) or the T416A mutation (Fig. 3d–f), consistent with the previous finding that these neurons express Gq-coupled mAChRs[47]. Thus, CKAR3, with its improved dynamic range, is sufficient for detecting PKC activity driven by mAChRs in CA1 neurons.
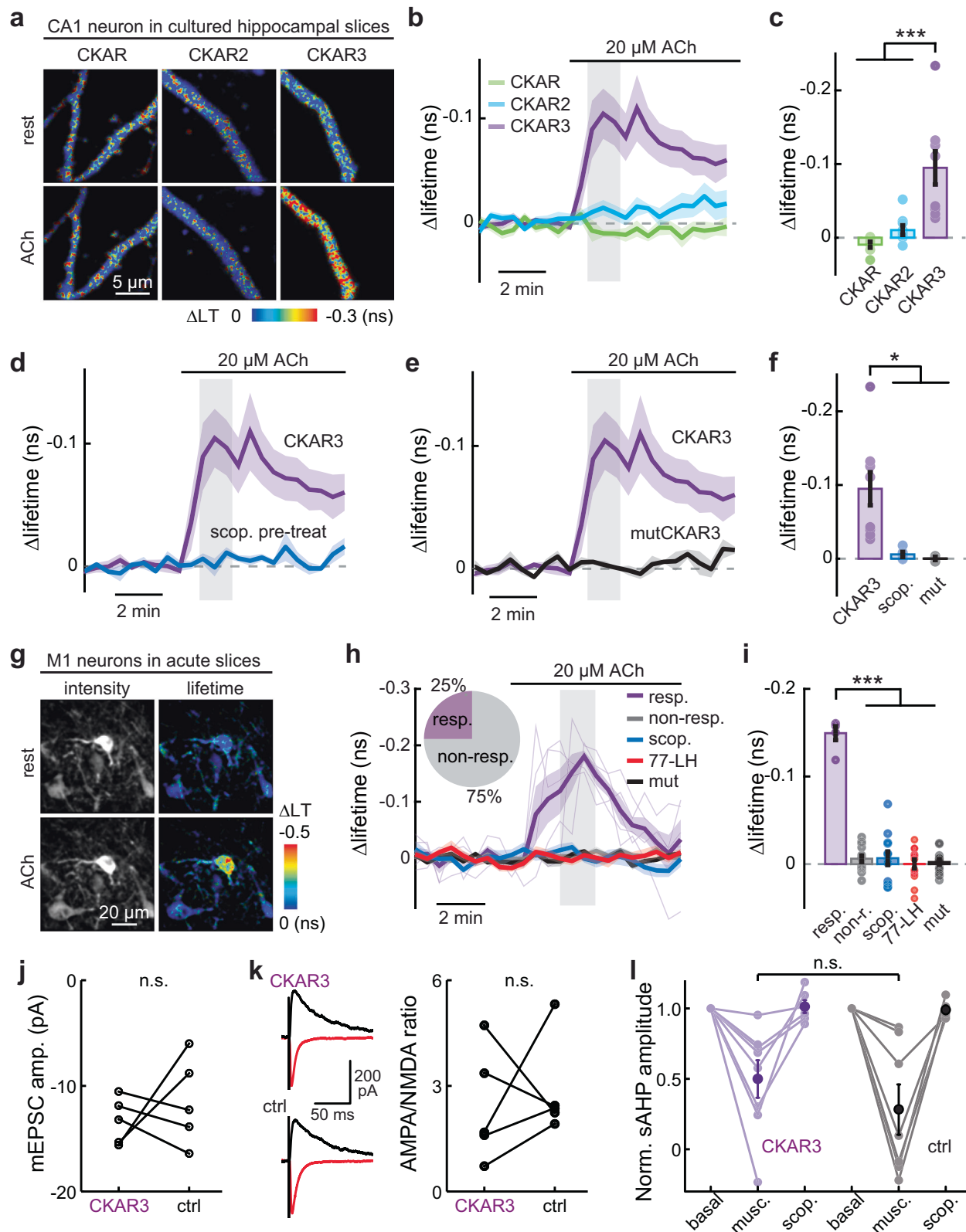
To test CKAR3's responses in cortical neurons, we expressed it in the mouse motor cortex via adeno-associated virus (AAV) injection. Layer 5 (L5) neurons were imaged in acute slices 20–25 days post infection. The sensor expressed well (Supplementary Fig. 5), and it responded to bath-applied acetylcholine in a subset (~25%) of imaged L5 neurons (Fig. 3g–i). This response was abolished by sco-polamine or the T416A mutation. Additional experiments showed

that the scopolamine effect could be recapitulated by 77-LH-28-1 (Fig. 3h, i), suggesting that the response was mediated by M1 mAChRs.

To determine whether CKAR3 expression may alter neuronal function, we performed whole-cell patch-clamp recordings from pyramidal neurons in the motor cortex in acute brain slices. CKAR3 expression did not alter neuronal properties that may be

Fig. 3 | Characterization of CKAR3 in neurons from brain slices. Representative images (**a**), average traces (**b**), and quantification (**c**) of CKAR sensors responding to acetylcholine (Ach, 20 μM) in CA1 neurons of cultured slices. *n* (cells) = 7, 9,9 for CKAR, CKAR2, CKAR3, respectively. One-way ANOVA [$F_{(2, 22)}$ = 14.11, *p* = 0.0001] with Bonferroni post hoc test. (*p* = 2×10^{-4} and 1×10^{-3}, respectively). Response traces of CKAR3 in CA1 neurons to acetylcholine compared to pre-treatment with scopolamine (scop., 1 μM) (**d**), mutCKAR3 (**e**), and their quantifications (**f**). In panel (**f**) from left to right, *n* (cells) = 9, 5, and 3. One-way ANOVA [$F_{(2, 14)}$ = 6.73, *p* = 0.009] with Bonferroni post hoc test [*p* = 0.02 and 0.04, respectively]. Representative images (**g**), average traces (**h**), and collective quantifications (**i**) of CKAR3 in M1 neurons in response to acetylcholine (responders are threshold 2x baseline s.d.) or with scopolamine pretreatments (blue), or mutCKAR3 responding to acetylcholine. In panel (**i**) from left to right, n (cells/mice) = 5/3, 15/3, 13/2, 14/2, and 15/3. One-way ANOVA [$F_{(4, 57)}$ = 70.74, *p* = 1.9×10^{-21}] with Bonferroni post hoc test. *p* = 0 for all

comparisons. **j** mEPSC amplitudes from paired adjacent L5 M1 pyramidal neurons with and without CKAR3 expression. *n* (pairs/mice) = 5/4, two-sided paired *t* test [$t_{(4)}$ = 0.7, *p* = 0.52]. **k** Representative recordings (left) at holding potential of −70 (red) and +55 (black) mV and quantified AMPA/NMDA receptor current ratios (right) from paired adjacent L5 M1 pyramidal neurons with and without CKAR3 expression. n (pairs/mice) = 5/2, [W = 9, *p* = 0.79], two-sided Wilcoxon signed-rank test. **l** Normalized amplitudes of slow afterhyperpolarizations (sAHPs) in response to a moderate concentration of muscarine (100 nM), with the majority followed by scopolamine (scop.) administrations, in CA1 neurons with and without CKAR3 expression. From left to right, n (cells/slices) = 8/8, 8/8, 6/6, 7/7, 7/7, and 5/5. Kruskal-Wallis test. n.s.: not significant [$H_{(1)}$ = 0.48, *p* = 0.51]. Mean (dark lines and bars) and s.e.m. (shaded area and error bars) are shown. n.s.: not significant, *: *p* < 0.05, **: *p* < 0.01, ***: *p* < 0.01. Source data are provided as a Source Data file.
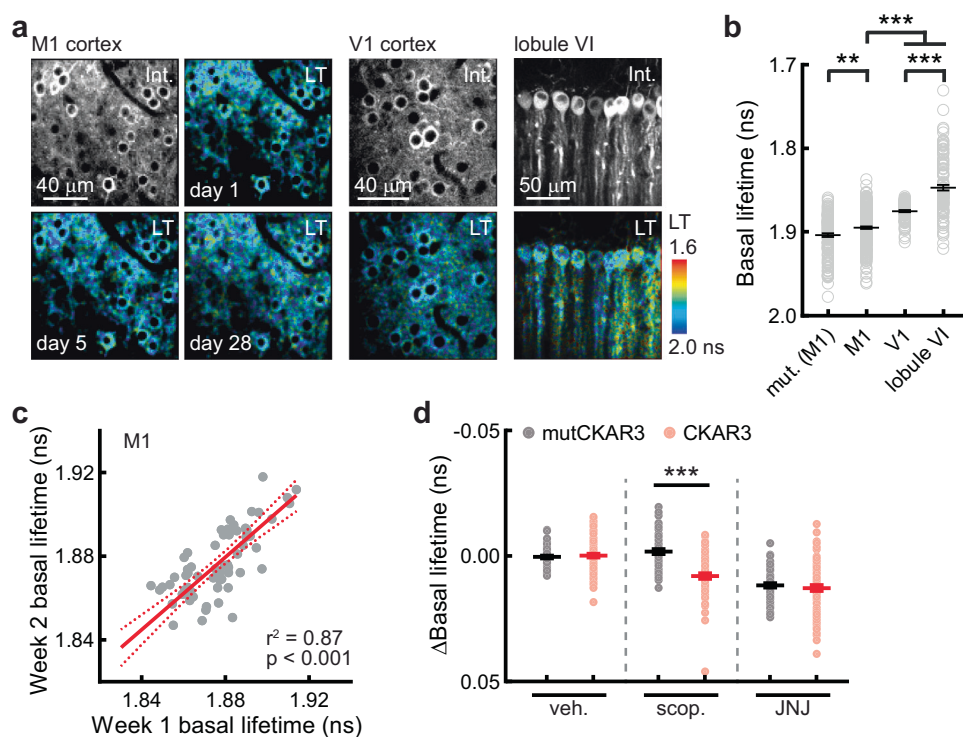

Fig. 4 | In vivo CKAR3 imaging revealed cell-specific, tonic PKC activity. Representative intensity and lifetime images (**a**) and quantifications of basal lifetimes (**b**) of CKAR3 or mutCKAR3 in L2/3 neurons of the M1 and V1 cortices and Purkinje cells of cerebellar lobule VI in awake mice, as indicated. LT: lifetime; int.: intensity. In panel (**b**) from left to right, n (cells/mice) = 132/7, 240/5, 82/3, and 110/3. For comparison between mut. (M1) and M1, two-sided Mann–Whitney U test was used [U = 13087, *p* = 0.006]; for comparison among M1, V1 and lobule VI, Kruskal-Wallis test [$H_{(2)}$ = 173.6, *p* = 3.2×10^{-38}] followed by corrected Dunn's post hoc test [M1 vs. V1: *p* = 2.4×10^{-9}, M1 vs. lobule VI: *p* = 1.1×10^{-37}, V1 vs. lobule VI: *p* = 4.2×10^{-6}]

was used. **c** Correlation of basal lifetimes with linear fit (solid line) and 95% confidence intervals (dashed lines) of the same M1 neurons across approximately a week. n (cells/mice) = 65/4, *p* = 3.2×10^{-13}, F-test. **d** Basal lifetime change of CKAR3 and mutCKAR3 induced by indicated drugs. From left to right, n (cells) = 60, 85, 60, 84, 60, and 70 from 4 mice. Two-sided Mann–Whitney U test was used [veh.: U = 2535, *p* = 0.95; scop.: U = 848, *p* = 4.4×10^{-10}; JNJ: U = 2420, *p* = 0.69]. Throughout the figure, horizontal black lines indicate mean and s.e.m.; **: *p* < 0.01, ***: *p* < 0.001. Source data are provided as a Source Data file.

regulated by PKC, such as the amplitude of miniature excitatory postsynaptic currents (mEPSCs)[48] and the AMPA and NMDA receptor current ratio[49] (Fig. 3j, k, and Supplementary Fig. 6a). The frequency of mEPSCs, paired-pulsed ratio (PPR), and the intrinsic excitability of cortical neurons were also unaffected (Supplementary Fig. 6a–j). Additionally, by using perforated patch on CA1 neurons of cultured hippocampal slices, we found that Gq-dependent regulation of the slow afterhyperpolarization by mAChRs[50–52] was not altered (Fig. 3l and Supplementary 6k, l). Overall, we concluded that CKAR3 enables the detection of PKC response to neuromodulators without affecting neuronal function.

In vivo imaging of CKAR3 revealed tonic PKC activity in cortical neurons

We asked whether CKAR3 was sufficient for in vivo imaging. It expressed well in vivo via AAV injection and could be imaged longitudinally in awake mice in all tested brain regions, including the primary motor cortex (M1), the primary visual cortex (V1), and the lobule VI of the cerebellum (Fig. 4a). MutCKAR3 exhibited comparable lifetimes between HEK cells (34 °C) and in M1 layer 2/3 neurons in vivo (Supplementary Fig. 7), verifying the stability of lifetime readouts across conditions and indicating that the sensor folding and integrity are consistent in vitro versus in vivo. Different brain regions exhibited different basal lifetimes, but they were all slightly shorter than those of

mutCKAR3 (Fig. 4b), indicating a tonic level of PKC activity in these neurons. The basal lifetimes of individual neurons were highly correlated week to week (Fig. 4c), suggesting that different brain regions and neurons exhibit distinct set points of basal PKC activity. We asked which pathways contributed to this basal PKC activity. Blockade of mAChR by scopolamine (1 mg/kg) moderately decreased CKAR3 activity compared to mutCKAR3 controls; whereas the metabotropic glutamate receptor antagonist JNJ16259685 (4 mg/kg) had no detectible effects compared to mutCKAR3 controls (Fig. 4d). Overall, these results indicate that 2pFLIM imaging of CKAR3 is sufficient to detect PKC activity in vivo.

Enforced locomotion elicited heterogeneous PKC responses across neurons

To test whether CKAR3 is sufficient to reveal behaviorally relevant PKC response, we used an enforced animal locomotion paradigm, which is known to be associated with increased arousal and the release of Gq-coupled neuromodulators[53–55]. Enforced locomotion elicited robust and repeatable PKC activity responses in a subset (~ 31%) of neurons in the M1 cortex but not in the V1 cortex or lobule VI of the cerebellum or when mutCKAR3 was used (Fig. 5a–f and Supplementary Fig. 8). This sparsity of responders is notably different from that for PKA activities under locomotion, in which a majority of M1 cells responded[31]. The responders could be separated into two distinct ensembles (Fig. 5g and Supplementary Fig. 9a). A silhouette analysis of the clustering quality also showed that two clusters gave the highest score (Supplementary Fig. 9b). The first cluster exhibited a fast-onset, transient response upon the start of locomotion (Fig. 5h). In contrast, neurons in the second cluster were gradually recruited with a delay from locomotion onset, and often exhibited multiple response peaks until the end of locomotion (Fig. 5h, i). These results reveal previously unappreciated, cell-specific heterogeneity in PKC signaling during animal behavior. By isolating and averaging the on- and off-traces of each response peak, we found that both clusters exhibited comparable on- and off-kinetics, with a τ_{on} of ~4 s and a τ_{off} of ~14 s (Fig. 5j).

Finally, we interrogated the upstream receptor mechanism of locomotion-elicited PKC activity using pharmacological manipulations. The PKC responses were dramatically reduced by the mAChR antagonist scopolamine, but not affected by mGluR antagonist JNJ16259685 (Fig. 5k). The effect of scopolamine was not due to decreased locomotive ability, as it did not significantly alter the ability of animals to move (Supplementary Fig. 10a; see "Methods"). Additionally, the two clusters of responder neurons exhibited similar pharmacological sensitivity (Supplementary Fig. 10b). These results indicate that mAChRs plays a major role in regulating both basal and locomotive PKC activities.

Discussion

Here, we report a next-generation lifetime PKC activity sensor, CKAR3. 2pFLIM imaging of CKAR3 enables in vivo PKC activity imaging and revealed basal PKC activity present in cortical neurons. Sparse, but robust, PKC dynamics were elicited during animal locomotion that were brain region-specific and largely dependent on mAChR signaling.

CKAR3 exhibits a > 10-fold enhanced lifetime dynamic range compared to its parental sensor CKAR2. CKAR3 was similar to tAKARβ[31] except for the substrate sequence, suggesting that the fluorescent protein pairs and their linker sequences in tAKARβ and CKAR3 may be a broadly applicable framework for developing additional kinase sensors. Regardless of the improvement mechanism, this enhanced dynamic range is critical. A tenfold increased signal tolerates a tenfold larger noise to achieve the same signal-to-noise ratio. Because the noise in determining lifetime is inversely proportional to the square root of the number of collected photons[31,56], this corresponds to a 100-fold decreased demand in the photon budget. In

practice, only CKAR3, but not CKAR or CKAR2, responded to acetylcholine application in cultured hippocampal slices (Fig. 3b). It also enables the examination of the direct response of neurons to the Gq-coupled GPCR pathway in vivo in single trials with a high signal-to-noise ratio. Moreover, we have observed both increased and decreased PKC dynamics via behavior and pharmacological manipulations, respectively, indicating that the sensitivity of CKAR3 is within the relevant range for PKC function.

CKAR3 detects the activity of multiple PKC isoforms (Fig. 2b). Its imaging therefore allows one to broadly visualize the integrated PKC activity from multiple upstream Gq pathways. The exact PKC isoform or upstream modulator can be further dissected by pairing with pharmacological manipulation using specific antagonists, as was done in recent studies that used in vivo PKA imaging to dissect upstream neuromodulatory mechanisms[31,32,57–61]. It is also important to note that the phosphorylation deficient mutant sensor (i.e., mutCKAR3) should be routinely used to control for potential response to unforeseen factors unrelated to phosphorylation.

We use in vivo 2pFLIM to image CKAR3. One key advantage of FLIM is its ability to quantify basal activity levels. We found a tonic PKC activity in cortical neurons of awake mice that is dependent on mAChRs. This activity is cell- and region-specific, and is stable over weeks, suggesting a controlled set point. This tonic PKC activity may enable a basal level of regulation on synaptic transmission and plasticity in specific neurons.

Intriguingly, we found that animal locomotion-elicited PKC responses were heterogeneous across brain regions, across different neurons in one region, and across responding neurons. This observed heterogeneity was not due to finite sensor sensitivity because all responders were detected with high signal-to-noise ratios. Although it is known that locomotion is associated with increased acetylcholine release in the cortex[53–55], which should in turn activate Gq-coupled receptors, the high degree of heterogeneity in the downstream effects was not previously known. While more work must be done to examine the mechanisms underlying these different levels of heterogeneity, we hypothesize that the cellular sparsity and distinct temporal properties (Fig. 5e, g) may be related to the integration of neuromodulatory and electrical signals in a specific subset of neurons, as postulated[23]. Regardless of the origin, the heterogeneity in the PKC pathway is noticeably different compared to our earlier result on PKA activity under locomotion in terms of brain regions, cell sparsity, and temporal properties[31]. The contrast highlights the differential activation of individual intracellular signaling pathways within a neuron and argues for the need for further tool development efforts to enable multiplex imaging of these pathways.

During the review process, another single-fluorophore PKC sensor, ExRai-CKAR2, was published[28]. We therefore compared CKAR3 with ExRai-CKAR2 and IDOCKS in HEK cells (Supplementary Fig. 11). As expected, ExRai-CKAR2 did not show lifetime responses (Supplementary Fig. 11a–c), although it exhibited larger fluorescence intensity changes than CKAR3 and IDOCKS did (Supplementary Fig. 11e). When using the respective imaging modality (see "Methods"), CKAR3 and ExRai-CKAR2 exhibit comparable signal-to-noise ratios and sensitivity in HEK cells (Supplementary Fig. 11e, f). We also compared CKAR3 and ExRai-CKAR2 in vivo based on their exhibited signal-to-noise ratio. Using an arbitrary threshold of 5x standard deviation of baseline, three times more cells expressing CKAR3 exhibited responses to enforced locomotion compared to cells expressing ExRai-CKAR2. Moreover, CKAR3 responses exhibited higher signal-to-noise ratios on average (Supplementary Fig. 12).

Overall, CKAR3 represents a major advancement for investigating PKC activity in vitro and in vivo. In addition to its physiological roles[16–23], defective PKC function has been associated with neurodegenerative diseases, such as Alzheimer's disease and spinocerebellar ataxia[62–66]. PKC activity imaging should contribute to a more detailed
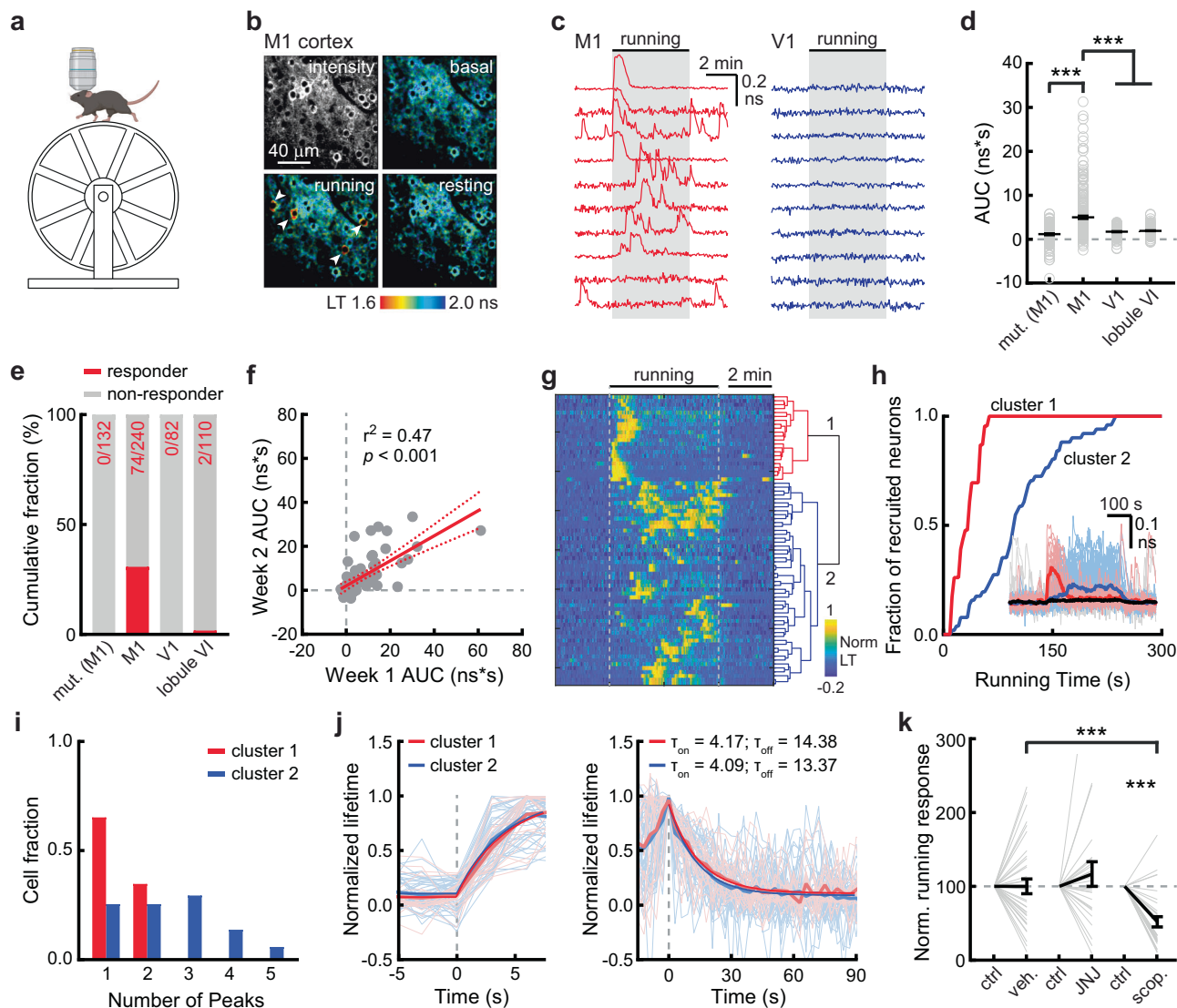
Fig. 5 | CKAR3 imaging revealed robust cell-specific PKC activity elicited by behavior. a Schematic imaging during enforced running. Created in BioRender. Yahiro, T. (2025) https://BioRender.com/ptch4h3. Representative images (**b**) and example traces (**c**) of CKAR3 in L2/3 M1 or V1 neurons during enforced running. Quantification (**d**) and fraction of responders (**e**, threshold 5x baseline s.d.) of L2/3 or Purkinje neurons expressing CKAR3 or mutCKAR3 in the indicated brain regions responding to enforced running. n (cells/mice) = 132/7, 240/5, 82/3, and 110/3. Kruskal-Wallis test [$H_{(3)}$ = 109.6, p = 3.1 × 10^{-24}] followed by corrected Dunn's post hoc test [M1 vs. mut. (M1): p = 1.2 × 10^{-20}, M1 vs. V1: p = 1.3 × 10^{-9}, M1 vs. lobule VI: p = 1.1 × 10^{-9}, V1 vs. lobule VI: p = 1.0] was used. **f** Correlation of AUC with the linear fit (solid line) and 95% confidence intervals (dashed lines) in the same L2/3 M1 neurons during enforced running across approximately one week. n (cells/mice) = 65/4, p = 1.4 × 10^{-10}, F-test. **g** Hierarchical clustering of the responses of 74 responder neurons. **h** Cumulative responder fractions over time of each cluster. Inset: traces and their average of each cluster or non-responders. n (cells) = 22 for cluster 1, 52 for cluster 2, and 168 for non-responders from 5 mice. **i** Fraction of neurons of each cluster with indicated number of responding peaks during the bouts. **j** On- and off-kinetics of CKAR3 in L2/3 M1 neurons. τ_{on} and τ_{off}: time constant of on- and off-kinetics. Exponential fitting curves for Cluster 1 (red) and Cluster 2 (blue) overlay average lifetime traces (bold light red and light blue, respectively), with individual neuron traces (thin light red and light blue lines, respectively). **k** CKAR3 response change to enforced running induced by indicated drugs. Note that only responders are included. From left to right, n (cells) = 35, 26 and 30 from 4 mice. Two-sided Wilcoxon signed-rank test for paired test [veh.: W = 35, p = 0.67; JNJ: W = −37, p = 0.65; scop.: W = 409, p = 3.7 × 10^{-6}]; Kruskal-Wallis test [$H_{(2)}$ = 18.39, p = 1.0 × 10^{-4}] followed by corrected Dunn's post hoc test [veh. vs. JNJ: p = 1, veh. vs. scop.: 7.9 × 10^{-4}] was used for comparison across groups. Throughout the figure, bold lines indicate mean and error bars indicate s.e.m.; ***: p < 0.001. Source data are provided as a Source Data file.

and nuanced understanding of cellular responses to neuromodulators and offer expanded opportunities for both basic research and therapeutic development.

Methods

Ethical statement

All surgical and experimental procedures were performed in accordance with the recommendations in the Guide for the Care and Use of Laboratory Animals, written by the National Research Council (US) Institute for Laboratory Animal Research, and were approved by the Institutional Animal Care and Use Committee (IACUC) of the Oregon Health and Science University (#IP00002274).

Plasmid constructs and virus production

Constructs were made using standard mutagenesis and subcloning methods, or by gene synthesis (Genewiz). CKAR3 has the same FHA1 domain and PKC substrate sequences as CKAR2, but different FPs and some differences in the linker region. Sensor constructs and their sequences have been deposited to Addgene. AAV2/1 viruses were packaged by NeuroTools (https://neurotools.virus.works). The viruses

express the sensor or mutant either under the human synapsin promotor or, when the Cre-dependent FLEX control is implemented, under a CAG promotor.

Cell culture and transfection

HEK-293 cells were obtained from American Type Culture Collection (ATCC #CRL-1573). Note that all cells from ATCC have been authenticated by morphology, karyotyping, and PCR-based approaches and tested for mycoplasma. Cell aliquots (within 2–4 passages) were kept frozen in liquid nitrogen until use. Thawed cells were further authenticated within the lab based on their morphology and growth characteristics and were maintained in 100-mm cell culture dishes (Fisher Scientific, #FB012924) at 37 °C with 5% CO_2 in minimal essential medium (ThermoFisher #11095-080) with the addition of 10% fetal bovine serum. Each aliquot of cells was passed and used for no more than 4 months.

To image transfected HEK cells under our two-photon microscope, cells were subcultured onto glass coverslips (~5 × 5 mm, hand-cut using a scriber) coated with 0.1 mg/mL Poly-D-Lysine (Sigma, #27964-99-4) in 35-mm cell culture dishes (Corning, #CLS430165), or seeded in 4-Chamber 35-mm glass bottom dishes (Cellvis, #D35C4-20-1.5-N). For sensor expression, constructs in mammalian expression plasmids (0.5 μg/35-mm dish unless otherwise noted) were transiently transfected using Lipofectamine-2000 (ThermoFisher, #11668030) according to the manufacturer's instructions with the exception that only 3 μl of the reagent was used. ITRACK and IDOCKS (both were the PKCα variant) were transfected with 0.5 μg of the donor construct with at 1:3 donor-acceptor ratio for ITRACK and 1:2 ratio for IDOCKS. For kinetics experiments, cells were transfected with 0.5 μg CKAR3 and 0.25 μg hM3D (i.e., Gq-coupled DREADD). A single-fluorophore PKC sensor ExRai-CKAR[24], which did not express well in our expression system and was not expected to exhibit lifetime changes, was not included in the comparison. Imaging was performed at two days post-transfection in a chamber perfused with carbogen (95% O_2/5% CO_2) gassed artificial cerebral spinal fluid (aCSF) containing (in mM) 127 NaCl, 25 NaHCO₃, 25 D-glucose, 2.5 KCl, 1.25 NaH₂PO₄, 2 CaCl₂, and 1 MgCl₂. An exception was that the experiments in Supplementary Fig. 10 were performed in HEPES buffered (25 mM, pH 7.4) HBSS solution (Gibco #14025). Drugs were bath-applied with the exception that C21 (0.5 mg/mL) was puffed using a Picospritzer II apparatus (16 psi) for the kinetics experiments.

Hippocampal slice culture and transfection

Hippocampi were dissected from P6–7 rat pups of both sexes. Sections (400 μm) were prepared using a chopper in dissection medium containing (in mM) 1 CaCl₂, 5 MgCl₂, 10 glucose, 4 KCl, 26 NaHCO₃, and 248 sucrose, with the addition of 0.00025% phenol red. The slices were then seeded onto a cell culture insert (Millipore, #PICM0RG50) and cultured at 35 °C with 5% CO_2 in 7.4 g/L MEM (ThermoFisher, #11700-077) with the addition of (in mM unless labeled otherwise): 16.2 NaCl, 2.5 L-Glutamax, 0.58 CaCl₂, 2 MgSO₄, 12.9 D-glucose, 5.2 NaHCO₃, 30 HEPES, 0.075% ascorbic acid, 1 mg/mL insulin, and 20% heat-inactivated horse serum. Slice media were refreshed every 2–3 days after seeding replacing ~60% of the culture media.

Transfection of cultured slices was accomplished using the biolistic method (Bio-Rad Helios gene gun) 10–20 days after seeding. In short, slices were bombarded with biolistic particles created by coating 1.6 μm gold particles (Bio-Rad, #165-2262; ~1 μg DNA/mg gold) with constructs in mammalian expression plasmids. Cultured slices were imaged at 2–3 days post-transfection in a chamber perfused with carbogen-gassed aCSF that contained 4 mM CaCl₂ and 4 mM MgCl₂. For physiology experiments, cultured slices were transfected using viral injection 6–7 days after seeding, and cultured neurons were recorded 12–20 days after injection.

Animal surgeries

C57BL/6 mice (both sexes from Charles River or home-bred within 5 generations from Charles River breeders) and *Pcp2-Cre* mice (Jax#010536; both sexes; for cerebellum labeling) were used. Mice were housed in a 12-h light/dark cycle at 22 °C and 30–70% humidity. Experiments were conducted during the light cycle. Surgeries were performed between p30 and p90 and mice were imaged until p300. Mice were transfected by stereotaxic viral injection, as previously described[67,68]. Cranial window surgeries were performed as previously described[32,69]. Briefly, a circular craniotomy (~3.5 mm in diameter) was performed using an air-powered high-speed dental handpiece (Maxima Pro 2) and a ¼ inch carbide burr (Henry Schein #5701072) above the region of interest. 100 nL of AAV was then injected into multiple locations within the craniotomy with the following coordinates (in mm anterior to the bregma, lateral to the midline, below the pia): for the M1 motor cortex, (0.0, 1.0, 0.4), (0.5, 1.5, 0.4), and (1.0, 2.0, 0.4); for the V1 visual cortex: (−3.0, 2.5, 0.4), (−3.5, 2.5, 0.4), and (−4.0, 2.5, 0.4); for the lobule VI of the cerebellum, (−6.0, 0.0, 0.2–0.25) and (−6.5, 0.0, 0.2–0.25). The window and headplate were adhered to the skull using dental acrylics. Mice were treated with pre-operative dexamethasone (20 mg/kg) and post-operative carprofen (5 mg/kg) to reduce inflammation and were allowed to recover for at least two weeks before imaging.

Acute slice preparation

Mice aged p17-25, with neurons transfected via stereotaxic AAV injection (0.65 mm lateral, 1 mm anterior to bregma, 0.35 mm deep), were perfused with ice-cold, gassed aCSF. The brain was then resected and sliced in a 10-degree tilted coronal plane using a vibratome (Leica VT1200s) in an ice-cold, gassed choline-cutting solution containing (in mM): 110 choline chloride, 25 NaHCO₃, 25 D-glucose, 2.5 KCl, 7 MgCl₂, 0.5 CaCl₂, 1.25 NaH₂PO₄, 11.5 sodium ascorbate, and 3 sodium pyruvate. The slices were then incubated in carbogen-gassed aCSF at 35 °C for 30 min and subsequently kept at room temperature for up to 12 h.

Electrophysiology

CA1 pyramidal neurons in cultured hippocampal slices were recorded using the gramicidin-perforated current clamp method. Transfected and untransfected neurons were recorded in separate slices on similar days in culture (DIC 18-26 for transfected, DIC 20-27 for untransfected). Culture slices were perfused at room temperature with gassed aCSF containing (in mM) 126 NaCl, 26 NaHCO₃, 10 D-glucose, 2.5 KCl, 1.25 NaH₂PO₄, 4 CaCl₂, and 4 MgCl₂ (~290 mOsm/kg, ~7.3 pH). Electrodes for perforated patch recording were filled with a solution containing (in mM) 140 KMeSO₄, 10 HEPES, and 7.5 NaCl (~300 mOsm/kg, ~7.3 pH, adjusted with KOH). Pipettes (4–8 MΩ) were pulled from borosilicate glass (G150F-3; Warner Instruments) using a model P-1000 puller (Sutter Instruments), front-filled with the internal, then back-filled with the same internal containing ~25 μg/mL Gramicidin (Sigma). After a seal was established, 10-45 min were allowed to gain sufficient access for current-clamp recording (40-80 MΩ) using the active bridge circuit of a Multiclamp 700B amplifier (Molecular Devices). The output was filtered at 10 kHz before being digitized at 20 kHz. To prevent recurrent excitation and block synaptic inputs, these recordings were made in the presence of (in μM) 10 NBQX, 10 CPP, and 10 gabazine. CA1 pyramidal neurons were selected based on their location and morphology, with a bias towards neurons with a long, intact apical dendrite, as those exhibit large slow afterhyperpolarizations (sAHPs)[70]. CA1 neurons were further verified based on their resting membrane potentials (−70 ± 3 mV and −70 ± 4 mV for transfected and untransfected neurons, respectively), first approximations of their whole-cell capacitance (147 ± 53 and 182 ± 47 pF for transfected and untransfected neurons, respectively), and their delayed ramp to spike following a simple 1 s current step. Slow AHPs were evoked by driving ten action potentials in quick succession with ten brief pulses (2 ms,

1500–2500 pA, 40 Hz). Access resistance was monitored carefully throughout the entire course of the experiment. Any quick drop in access was interpreted as membrane rupture, and recording was ended.

Layer 5 pyramidal neurons in acute slices of the motor cortex were recorded using the whole-cell patch-clamp technique. Transfected and adjacent (within 100 μm) untransfected neurons were recorded sequentially. Voltage- and current-clamp recordings were performed using a MultiClamp 700B amplifier (Molecular Devices) controlled by a software package (yphys_StimScope) written in MATLAB kindly provided by Dr. Ryohei Yasuda. Electrophysiological signals were filtered at 2 kHz before being digitized at 20 kHz. Slices were perfused at 33–35 degrees Celsius with gassed aCSF containing 2 mM $CaCl_2$ and 2 mM $MgCl_2$. Recording pipettes (3–5 MΩ), were pulled from borosilicate glass (G150F-3; Warner Instruments) using a model P-1000 puller (Sutter Instruments). Series resistances were 8–26 MΩ. The internal solution contained (in mM): 128 K-gluconate, 4 $MgCl^2$, 10 HEPES, 10 Na-phosphocreatine, 3 Na-L-ascorbate, 0.4 Na-GTP, 4 Na-ATP, 1 EGTA and 4 QX-314 bromide (303 mOsmol/kg, pH 7.24, adjusted with CsOH). Voltages were not corrected for the liquid junction potential.

Monosynaptic excitatory postsynaptic currents (EPSCs) were evoked by extracellular stimulation of axons in the motor cortex using a theta-glass (20–50 μm tip) electrode filled with aCSF and positioned ~200 μm ventral from somata. Short (0.1 ms), weak (25–500 μA) pulses were applied using an A365 stimulus isolator (World Precision Instruments). Direct activation of the recorded neuron was prevented by blocking action potentials with 4 mM QX-314 in the internal solution. $GABA_A$ currents were blocked by adding 50–100 μM picrotoxin in the bath. In voltage-clamp mode, cells were first held at –70 mV to record AMPA currents and then at +55 mV to record NMDA currents. AMPA/NMDA ratios were calculated as the peak amplitudes of currents evoked at –70 mV divided by the average amplitudes of currents evoked at +55 mV, 40–50 ms after stimulation. Paired-pulse ratios (PPRs) were calculated as the ratio between the amplitudes of two EPSCs (2nd peak/1st peak) evoked by electrical stimuli separated by 70 ms while holding the cell at –70 mV. 10–20 trials were recorded with an interstimulus interval of 10 s.

Miniature EPSCs were recorded in the presence of 1 μM TTX, 10 μM CPP, and 100 μM picrotoxin (to block action potentials, NMDA receptors, and $GABA_A$ receptors, respectively). mEPSCs were detected as negative deflections that exceeded 5 times the median absolute value of the smoothed first derivative of the current traces. Input resistance was calculated from a test pulse in voltage-clamp mode. In current-clamp mode, instantaneous firing rates were calculated as the inverse of the first interspike interval following current injection, and steady-state firing rates were calculated as the inverse of the average interspike interval in the last half of a 1 s current injection.

Two-photon and 2pFLIM imaging

The in vitro two-photon microscope was built as previously described[71] and the in vivo two-photon microscope was built based on the open-access design of the Modular In vivo Multiphoton Microscopy System (MIMMS) from Howard Hughes Medical Institute Janelia Research Campus (https://www.janelia.org/open-science/mimms). FLIM capacity was added as previously described[31,69]. Briefly, A photodiode (Thorlabs FDS010) was added to detect the arrival of the laser pulses. The output of a fast photomultiplier tube (Hamamatsu H7422PA-40, H10769PA-40, or H10770A-40) was compared with laser pulse timing using a TCSPC-730 (Becker and Hickl), or TimeHarp 260 (PicoQuant) time-correlated single photon counting board. Experiments using TCSPC-730 were controlled by the ScanImage software[71] (Vidrio, version 3.5) integrated with a modified add-on called FLIMimage (version 1.0), which was written in MATLAB and was kindly provided by Dr. Ryohei Yasuda. Experiments using TimeHarp were controlled by FLIMage (Florida Lifetime Imaging, version 4.0.3α). Fluorophores were

excited with a pulsed 80 MHz Titanium-Sapphire laser at the following wavelengths: (850 nm for CKAR and CKAR2; 920 nm for ITRACK and IDOCKS; and 960 for CKAR3, mutCKAR3, and KCP). The fluorescence emission was unmixed using a dichroic mirror and band-pass filters. Specifically, Semrock FF511-Di01, Semrock FF01-483/32, and Semrock FF01-550/49 were used for CKAR, CKAR2, and additional CKAR variants and for ratiometric imaging of KCP. The Chroma 565DCXR dichroic with Semrock FF01-630/92 and Chroma HQ510/70 barrier filters was used for ITRACK, IDOCKS, and CKAR3, and for lifetime imaging of KCP.

For Supplementary Fig. 11, cells plated on glass-bottom dishes were imaged on a custom-built inverted 2pFLIM microscope with hardware specification similar to the in vitro 2pFLIM microscope described above except that a TCSPC-150N board (Becker and Hickl) was used. Fluorophores were excited with a Coherent Chameleon Ultra laser at 920 nm, and fluorescence was collected with Chroma ET510/40m-2p and Chroma ET620/60m-2p emission filters. To compare signal-to-noise ratio across groups in Supplementary Fig. 10, plasmid transfection conditions and imaging settings were kept consistent for IDOCKS, CKAR3, and ExRai-CKAR2.

During imaging experiments, animals were head-fixed and placed on a one-dimensional treadmill that was fixed except during locomotion-related experiments. CKAR3 and mutCKAR3 were excited at 920 nm. For Supplementary Fig. 12, ExRai-CKAR2 was excited at 960 nm, which was necessary to distinguish the cells from the background. Enforced-running experiments were carried out using a motorized treadmill set to a velocity of approximately 5 cm/s at the indicated time. For the pharmacological experiment, the mouse was first exposed to the enforced running described above and then administered drugs via subcutaneous (s.c.) injection 30 min before the enforced running. JNJ16259685 (JNJ: Tocris) was dissolved in DMSO at 10 mg/mL and then diluted in saline to final concentration of 1 mg/mL. Scopolamine (scop: Tocris) was dissolved in saline at final concentration of 250 μg/mL. JNJ and scopolamine were subcutaneously administered at the dose of 4 mg/kg and 1 mg/kg, respectively. Saline was administered as the vehicle control. The animal behavior was video recorded using a camera (ELP, #USBFHD05MT-KL156IR), and the number of steps was visually counted.

Spectrum determination

For measuring the one-photon emission spectra, cells were imaged 48 h after transfection first in the absence and then in the presence of 1 μM PDBu and ionomycin. A Zeiss LSM 880 was used to collect the emission spectrum of CKAR3 in situ. A laser of 458 nm was used for excitation and the emission spectrum was then measured at 4.5-nm increments ranging from 464 to 652 nm using the built-in 34-channel spectrum detector. The two-photon excitation spectra of CKAR3 and mEGFP were measured at 20-nm increments ranging from 840 to 1040 nm except that 930 nm was used in place of 940 nm using the inverted 2pFLIM microscope. The laser power was determined at each wavelength at the sample plane using a power meter. Comparable powers (3.0–3.4 mW) were used across the wavelength range, and the signals were corrected for excitation power by dividing by the square of the imaging power. The fluorescence measured in non-transfected cells was subtracted as background and normalized to the peak value in the absence of PDBu and ionomycin.

Image analysis

Data analyses were performed using custom software written in MATLAB. In particular for 2pFLIM analyses, we used a software suite called FLIMview written in MATLAB[58]. Where appropriate, regions of interest were drawn to isolate individual HEK cells or neurons from contamination by background photons or adjacent cells/structures. For ratiometric imaging, individual channels were background subtracted based on a nearby background ROI before calculating the ratio.

Fluorescence lifetime was approximated by mean photon emission time τ in Eq.(1) below:

$$\tau = \langle t \rangle - t_0 \tag{1}$$

such that t reflects the emission time of individual photons in the measurement window and t_0 reflects the timing of laser pulses. t_0 is a fixed property of a given hardware configuration and is measured separately under ideal imaging conditions. Because the measurement window (t_w) is finite (≤ 10 ns passing t_0 due to laser pulse repetition and single photon counting hardware properties), the measured τ ($\tau_{apparent}$) is slightly smaller than the real value. For example, for a τ of 2.0 ns and a t_w of 9.0 ns, the $\tau_{apparent}$ is 1.90 following Eq.(2) below:

$$\tau_{apparent} = (\tau - (t_w + \tau) * e^{-\frac{t_w}{\tau}})/(1 - e^{-\frac{t_w}{\tau}}) \tag{2}$$

For the analysis of in vivo ExRai-CKAR2 signals in Supplementary Fig. 11, Suite2P[72] was used for x-y plane motion correction and cell detection.

Analysis of in vivo data

The basal lifetime of each cell was calculated as the mode of the distribution estimated by Kernel Density Estimation on the 5-min baseline. For Figs. 4c, 5f, linear regression was used to represent the correlation of basal lifetimes and area under curve (AUC) during enforced running within the same cells in the M1 cortex imaged 5–8 days apart. For Fig. 5g, hierarchical clustering using Ward's method was performed on the data normalized to the peak response of each responder cell to enforced running. The optimal number of clusters was determined based on the highest mean silhouette score (Supplementary Fig. 8b). For Fig. 5i, the data were smoothed using a moving average filter with a window size of 5, and peaks and their timing were detected as 3 times more than the standard deviation of the baseline in running sessions. For Fig. 5j, the on- and off-kinetics of each cluster were calculated using one-phase decay with least squares regression from data normalized to the first and last peaks of each cell, respectively. For Fig. 5k, the response to the enforced running after drug administration was normalized to the control response prior to the drug administration.

Statistics and reproducibility

Quantification and statistical tests were performed using MATLAB 2013b–2022a and GraphPad Prism 10.4.0. Averaged data are presented as mean ± s.e.m., unless noted otherwise. Example traces in Figs. 1–3 and ED Figs. 1, 3, 4, were smoothed using a running average filter with a window of 3 points. All measurements were taken from different cells. "n" refers to the number of cells unless noted. In HEK cell experiments, most experiments measured two (~ 70%) or three cells simultaneously per coverslip. In a few specific experiments (Fig. 2a and Supplementary Fig. 4, 10), up to 15 cells were imaged. In cultured slice experiments, all neurons except a pair came from different slices. In acute slice imaging experiments, 3–7 neurons were imaged per slice. All experiments were repeated for at least two, typically more, independent transfections (in vitro) or mice (in vivo). When representative images are shown, independent experiments with similar results were repeated at least two additional times. Due to the nature of testing a sensor with an unknown signal-to-noise ratio, no statistical method was used to pre-determine sample size. Experiments were not randomized and experimenters were not blinded to the treatment. Unless otherwise noted, the Shapiro-Wilk test was used to determine if data were normally distributed, and the Bartlett test was used to determine if variances were equal. When the assumptions of normality and homoscedasticity were met, a two-sided Student's t test or one-way ANOVA followed by a Bonferroni post hoc test were used. When the assumption of normality was not met, a two-sided Wilcoxon signed-

rank test, a two-sided Mann–Whitney U test and a Kruskal-Wallis test followed by corrected Dunn's post hoc test were used for paired and unpaired comparisons. In all figures, *: $p < 0.05$, **: $p < 0.01$, and ***: $p < 0.001$.

Reporting summary

Further information on research design is available in the Nature Portfolio Reporting Summary linked to this article.

Data availability

The sensor constructs and their corresponding sequences have been deposited to Addgene (http://addgene.org; #238411–238414). Source data are provided with this paper.

References

1. Greengard, P. The neurobiology of slow synaptic transmission. *Science* 294 at https://doi.org/10.1126/science.294.5544.1024 (2001).
2. Wettschureck, N. & Offermanns, S. Mammalian G proteins and their cell type specific functions. *Physiol. Rev.* 85 at https://doi.org/10.1152/physrev.00003.2005 (2005).
3. Marder, E. Neuromodulation of neuronal circuits: Back to the future. *Neuron* vol. 76 at https://doi.org/10.1016/j.neuron.2012.09.010 (2012).
4. Lee, S. H. & Dan, Y. Neuromodulation of brain states. *Neuron* 76 at https://doi.org/10.1016/j.neuron.2012.09.012 (2012).
5. Sarter, M. & Bruno, J. P. Cognitive functions of cortical acetylcholine: Toward a unifying hypothesis. *Brain Research Reviews* vol. 23 at https://doi.org/10.1016/S0165-0173(96)00009-4 (1997).
6. Hasselmo, M. E. The role of acetylcholine in learning and memory. *Curr. Opin. Neurobiol.* 16 at https://doi.org/10.1016/j.conb.2006.09.002 (2006).
7. Paul, S. M., Yohn, S. E., Popiolek, M., Miller, A. C. & Felder, C. C. Muscarinic acetylcholine receptor agonists as novel treatments for schizophrenia. *Am. J. Psychiatry* 179, 611-627 at https://doi.org/10.1176/appi.ajp.21101083 (2022).
8. Ballanger, B. et al. Serotonin 2A receptors and visual hallucinations in Parkinson disease. *Arch. Neurol.* **67**, 416–421 (2010).
9. Kometer, M., Schmidt, A., Jancke, L. & Vollenweider, F. X. Activation of serotonin 2A receptors underlies the psilocybin-induced effects on α oscillations, N170 visual-evoked potentials, and visual hallucinations. *J. Neurosci.* **33**, 10544–10551 (2013).
10. Geyer, M. A. & Vollenweider, F. X. Serotonin research: Contributions to understanding psychoses. *Trends Pharmacol. Sci.* 29 at https://doi.org/10.1016/j.tips.2008.06.006 (2008).
11. Dong, C. et al. Fluorescence imaging of neural activity, neurochemical dynamics, and drug-specific receptor conformation with genetically encoded sensors. *Ann. Rev. Neurosci.* 45 273–294 at https://doi.org/10.1146/annurev-neuro-110520-031137 (2022).
12. Sabatini, B. L. & Tian, L. Imaging neurotransmitter and neuromodulator dynamics in vivo with genetically encoded indicators. *Neuron* 108 17–32 at https://doi.org/10.1016/j.neuron.2020.09.036 (2020).
13. Wu, Z., Lin, D. & Li, Y. Pushing the frontiers: Tools for monitoring neurotransmitters and neuromodulators. *Nat. Rev. Neurosci.* 23 at https://doi.org/10.1038/s41583-022-00577-6 (2022).
14. Van Der Zee, E. A. & Douma, B. R. K. Historical review of research on protein kinase C in learning and memory. *Prog. Neuro-Psychopharmacol. Biol. Psychiatry* **21**, 379–406 (1997).
15. Callender, J. A. & Newton, A. C. Conventional protein kinase C in the brain: 40 years later. *Neuronal Signal* **1**, NS20160005 (2017).
16. Astman, N., Gutnick, M. J. & Fleidervish, I. A. Activation of protein kinase c increases neuronal excitability by regulating persistent Na+ current in mouse neocortical slices. *J. Neurophysiol.* **80**, 1547–1551 (1998).

17. Hoffman, D. A. & Johnston, D. Downregulation of transient K+ channels in dendrites of hippocampal CA1 pyramidal neurons by activation of PKA and PKC. *J. Neurosci.* **18**, 3521–3528 (1998).

18. Boehm, J. et al. Synaptic Incorporation of AMPA Receptors during LTP Is Controlled by a PKC Phosphorylation Site on GluR1. *Neuron* **51**, 213–225 (2006).

19. Lan, J. et al. Protein kinase C modulates NMDA receptor trafficking and gating. *Nat. Neurosci.* **4**, 382–390 (2001).

20. Lin, Y., Jover-Mengual, T., Wong, J., Bennett, M. V. L. & Zukin, R. S. PSD-95 and PKC converge in regulating NMDA receptor trafficking and gating. *Proc. Natl. Acad. Sci. Usa.* **103**, 19902–19907 (2006).

21. Chung, H. J., Xia, J., Scannevin, R. H., Zhang, X. & Huganir, R. L. Phosphorylation of the AMPA receptor subunit GluR2 differentially regulates its interaction with PDZ domain-containing proteins. *J. Neurosci.* **20**, 7258–7267 (2000).

22. Xia, J., Chung, H. J., Wihler, C., Huganir, R. L. & Linden, D. J. Cerebellar long-term depression requires PKC-regulated interactions between GluR2/3 and PDZ domain-containing proteins. *Neuron* **28**, 499–510 (2000).

23. Colgan, L. A. et al. PKCα integrates spatiotemporally distinct Ca 2+ and autocrine BDNF signaling to facilitate synaptic plasticity. *Nat. Neurosci.* **21**, 1027–1037 (2018).

24. Mehta, S. et al. Single-fluorophore biosensors for sensitive and multiplexed detection of signalling activities. *Nat. Cell Biol.* **20**, 1215–1225 (2018).

25. Violin, J. D., Zhang, J., Tsien, R. Y. & Newton, A. C. A genetically encoded fluorescent reporter reveals oscillatory phosphorylation by protein kinase C. *J. Cell Biol.* **161**, 899–909 (2003).

26. Ross, B. L. et al. Single-color, ratiometric biosensors for detecting signaling activities in live cells. *Elife* **7**, e35458 (2018).

27. Schleifenbaum, A., Stier, G., Gasch, A., Sattler, M. & Schultz, C. Genetically encoded FRET probe for PKC activity based on pleckstrin. *J. Am. Chem. Soc.* **126**, 11786–11787 (2004).

28. Su, Q. et al. Sensitive fluorescent biosensor reveals differential subcellular regulation of PKC. *Nat. Chem. Biol.* **21**, 501–511 (2024).

29. Colgan, L. A. et al. Dual regulation of spine-specific and synapse-to-nucleus signaling by PKCd during plasticity. *J. Neurosci.* **43**, 5432–5447 (2023).

30. Tu, X., Yasuda, R. & Colgan, L. A. Rac1 is a downstream effector of PKCα in structural synaptic plasticity. *Sci. Rep.* **10**, 1777 (2020).

31. Ma, L. et al. A highly sensitive A-kinase activity reporter for imaging neuromodulatory events in awake mice. *Neuron* **99**, 665–679.e5 (2018).

32. Massengill, C. I. et al. Sensitive genetically encoded sensors for population and subcellular imaging of cAMP in vivo. *Nat. Methods* **19**, 1461–1471 (2022).

33. Yasuda, R. et al. Supersensitive Ras activation in dendrites and spines revealed by two-photon fluorescence lifetime imaging. *Nat. Neurosci.* **9**, 283–291 (2006).

34. Yellen, G. & Mongeon, R. Quantitative two-photon imaging of fluorescent biosensors. *Curr. Opin. Chem. Biol.* 27 24–30 at https://doi.org/10.1016/j.cbpa.2015.05.024 (2015).

35. Durocher, D. et al. The molecular basis of FHA domain:Phosphopeptide binding specificity and implications for phospho-dependent signaling mechanisms. *Mol. Cell* **6**, 1169–1182 (2000).

36. Nishikawa, K., Toker, A., Johannes, F. J., Songyang, Z. & Cantley, L. C. Determination of the specific substrate sequence motifs of protein kinase C isozymes. *J. Biol. Chem.* **272**, 952–960 (1997).

37. Yaffe, M. B. et al. A motif-based profile scanning approach for genome-wide prediction of signaling pathways. *Nat. Biotechnol.* **19**, 348–353 (2001).

38. Goedhart, J. et al. Structure-guided evolution of cyan fluorescent proteins towards a quantum yield of 93. *Nat. Commun.* **3**, 751 (2012).

39. van der Krogt, G. N. M., Ogink, J., Ponsioen, B. & Jalink, K. A comparison of donor-acceptor pairs for genetically encoded FRET sensors: Application to the Epac cAMP sensor as an example. *PLoS One* **3**, e1916 (2008).

40. Ganesan, S., Ameer-Beg, S. M., Ng, T. T. C., Vojnovic, B. & Wouters, F. S. A dark yellow fluorescent protein (YFP)-based Resonance Energy-Accepting Chromoprotein (REACh) for Förster resonance energy transfer with GFP. *Proc. Natl. Acad. Sci. Usa.* **103**, 4089–4094 (2006).

41. Murakoshi, H., Lee, S. J. & Yasuda, R. Highly sensitive and quantitative FRET-FLIM imaging in single dendritic spines using improved non-radiative YFP. *Brain Cell Biol.* **36**, 31–42 (2008).

42. Chen, Y., Saulnier, J. L., Yellen, G. & Sabatini, B. L. A PKA activity sensor for quantitative analysis of endogenous GPCR signaling via 2-photon FRET-FLIM imaging. *Front. Pharmacol.* **5**, 56 (2014).

43. Jiang, Z. Y. et al. Insulin signaling through Akt/protein kinase B analyzed by small interfering RNA-mediated gene silencing. *Proc. Natl. Acad. Sci. USA* **100**, 7569–7574 (2003).

44. Atwood, B. K., Lopez, J., Wager-Miller, J., Mackie, K. & Straiker, A. Expression of G protein-coupled receptors and related proteins in HEK293, AtT20, BV2, and N18 cell lines as revealed by microarray analysis. *BMC Genomics* **12**, 14 (2011).

45. Reither, G., Schaefer, M. & Lipp, P. A versatile key for decoding the cellular calcium toolkit. *J. Cell Biol.* **174**, 521–533 (2006).

46. Erb, L. & Weisman, G. A. Coupling of P2Y receptors to G proteins and other signaling pathways. *Wiley Interdisciplinary Rev.: Membr. Transp. Signal.* 1 at https://doi.org/10.1002/wmts.62 (2012).

47. Giessel, A. J. & Sabatini, B. L. M1 muscarinic receptors boost synaptic potentials and calcium influx in dendritic spines by inhibiting postsynaptic SK channels. *Neuron* **68**, 936–947 (2010).

48. Carroll, R. C., Nicoll, R. A. & Malenka, R. C. Effects of PKA and PKC on miniature excitatory postsynaptic currents in CA1 pyramidal cells. *J. Neurophysiol.* **80**, 2797–2800 (1998).

49. Sun, L. & June Liu, S. Activation of extrasynaptic NMDA receptors induces a PKC-dependent switch in AMPA receptor subtypes in mouse cerebellar stellate cells. *J. Physiol.* **583**, 537–553 (2007).

50. Dutar, P. & Nicoll, R. Classification of muscarinic responses in hippocampus in terms of receptor subtypes and second-messenger systems: Electrophysiological studies in vitro. *J. Neurosci.* **8**, 4214–4224 (1988).

51. Krause, M., Offermanns, S., Stocker, M. & Pedarzani, P. Functional specificity of Gαq and Gα11 in the cholinergic and glutamatergic modulation of potassium currents and excitability in hippocampal neurons. *J. Neurosci.* **22**, 666–673 (2002).

52. Malenka, R., Madison, D., Andrade, R. & Nicoll, R. Phorbol esters mimic some cholinergic actions in hippocampal pyramidal neurons. *J. Neurosci.* **6**, 475–480 (1986).

53. Stobart, J. L. et al. Cortical circuit activity evokes rapid astrocyte calcium signals on a similar timescale to neurons. *Neuron* **98**, 726–735.e4 (2018).

54. Reimer, J. et al. Pupil fluctuations track rapid changes in adrenergic and cholinergic activity in cortex. *Nat. Commun.* **7**, 13289 (2016).

55. Collins, L., Francis, J., Emanuel, B. & McCormick, D. A. Cholinergic and noradrenergic axonal activity contains a behavioral-state signal that is coordinated across the dorsal cortex. *Elife* **12**, e81826 (2023).

56. Yasuda, R. Imaging spatiotemporal dynamics of neuronal signaling using fluorescence resonance energy transfer and fluorescence lifetime imaging microscopy. *Curr. Opin. Neurobiol.* 16 at https://doi.org/10.1016/j.conb.2006.08.012 (2006).

57. Zhang, S. X. et al. Hypothalamic dopamine neurons motivate mating through persistent cAMP signalling. *Nature* **597**, 245–249 (2021).

58. Ma, L., et al. Locomotion activates PKA through dopamine and adenosine in striatal neurons. *Nature* **611**, 762–768 (2022).

59. Lutas, A., Fernando, K., Zhang, S. X., Sambangi, A. & Andermann, M. L. History-dependent dopamine release increases cAMP levels in

most basal amygdala glutamatergic neurons to control learning. *Cell Rep.* **38**, 110297 (2022).

60. Lee, S. J. et al. Cell-type-specific asynchronous modulation of PKA by dopamine in learning. *Nature* **590**, 451–456 (2021).

61. Singh Alvarado, J. et al. Transient cAMP production drives rapid and sustained spiking in brainstem parabrachial neurons to suppress feeding. *Neuron* **112**, 1416–1425.e5 (2024).

62. Wang, H. Y., Pisano, M. R. & Friedman, E. Attenuated protein kinase C activity and translocation in Alzheimer's Disease brain. *Neurobiol. Aging* **15**, 293–298 (1994).

63. Cole, G., Dobkins, K. R., Hansen, L. A., Terry, R. D. & Saitoh, T. Decreased levels of protein kinase C in Alzheimer brain. *Brain Res.* **452**, 165–174 (1988).

64. Talman, V., Pascale, A., Jäntti, M., Amadio, M. & Tuominen, R. K. Protein Kinase C activation as a potential therapeutic strategy in Alzheimer's disease: Is there a role for embryonic lethal abnormal vision-like proteins? *Basic Clin. Pharmacol. Toxicol.* 119 at https://doi.org/10.1111/bcpt.12581 (2016).

65. Lordén, G. et al. Enhanced activity of Alzheimer disease-associated variant of protein kinase Cα drives cognitive decline in a mouse model. *Nat. Commun.* **13**, 7200 (2022).

66. Shirafuji, T. et al. Spinocerebellar ataxia type 14 caused by a nonsense mutation in the PRKCG gene. *Mol. Cell. Neurosci.* **98**, 46–53 (2019).

67. Hunnicutt, B. J. et al. A comprehensive thalamocortical projection map at the mesoscopic level. *Nat. Neurosci.* **17**, 1276–1285 (2014).

68. Mao, T. et al. Long-Range Neuronal Circuits Underlying the Interaction between Sensory and Motor Cortex. *Neuron* **72**, 111–123 (2011).

69. Jongbloets, B. C., Ma, L., Mao, T. & Zhong, H. Visualizing protein kinase A activity in head-fixed behaving mice using in vivo two-photon fluorescence lifetime imaging microscopy. *J. Vis. Exp.* https://doi.org/10.3791/59526 (2019).

70. Bekkers, J. M. Distribution of slow AHP channels on hippocampal CA1 pyramidal neurons. *J. Neurophysiol.* **83**, 1756–1759 (2000).

71. Pologruto, T. A., Sabatini, B. L. & Svoboda, K. ScanImage: Flexible software for operating laser scanning microscopes. *Biomed. Eng. Online* **2**, 13 (2003).

72. Pachitariu, M. et al. Suite2p: beyond 10,000 neurons with standard two-photon microscopy. *bioRxiv* https://doi.org/10.1101/061507 (2016).

Acknowledgements

Author contributions

H.Z. conceived the project and generated the initial variants. T.Y., L.B.E., J.A.J., Y.Z., T.M., and H.Z. designed the experiments. L.B.E., Y.Z., and H.Z. performed in vitro imaging experiments. T.Y. performed in vivo experiments with initial guidance from L.M. and assistance from H.Z. and L.B.E. JAJ performed electrophysiological recordings. M.Q. prepared and maintained cultured slices and conducted mouse husbandry. T.Y., L.B.E., J.A.J., Y.Z., and H.Z. analyzed the data. T.Y., L.B.E., J.A.J., Y.Z., T.M., and H.Z. wrote the manuscript, with edits and comments by all authors. T.M. and H.Z. secured the funding and supervised the project.

Competing interests

The authors declare no competing interests.

Additional information

Supplementary information The online version contains supplementary material available at https://doi.org/10.1038/s41467-025-61729-7.

Correspondence and requests for materials should be addressed to Tianyi Mao or Haining Zhong.

Peer review information *Nature Communications* thanks the anonymous reviewers for their contribution to the peer review of this work. A peer review file is available.

Reprints and permissions information is available at http://www.nature.com/reprints

Publisher's note Springer Nature remains neutral with regard to jurisdictional claims in published maps and institutional affiliations.